minerals

MDPI

Article

Effect of Cerium-Containing Hydroxyapatite in Bone Repair in Female Rats with Osteoporosis Induced by Ovariectomy

Ewerton Vieira [1,2], Marcos Silva [2], Antonio Maia-Filho [3], Daniel Ferreira [3], José Figuerêdo-Silva [3], Karla Rovaris [4], Ana Cristina Fialho [4], Ana Leite-Oliveira [5], André L. Menezes de Oliveira [6], Maria Gardênnia da Fonseca [6], Josy A. Osajima [2] and Edson C. da Silva-Filho [2,*]

1 Instituto Federal do Maranhão, Buriticupu MA 65393-000, Brazil; ewertonvieira@ufpi.edu.br
2 Interdisciplinary Laboratory of Advanced Materials, Federal University of Piaui, Teresina PI 64049-550, Brazil; marcosqps@hotmail.com (M.S.); josyosajima@ufpi.edu.br (J.A.O.)
3 Central Campus, State University of Piaui, Teresina PI 64000-040, Brazil; almmaiaf@gmail.com (A.M.-F.); dannielclf@hotmail.com (D.F.); figueredo_silva@hotmail.com (J.F.-S.)
4 Department of Pathology and Dental Clinic, Federal University of Piaui, Teresina PI 64049-550, Brazil; karlarovaris@gmail.com (K.R.); anacrisvf@gmail.com (A.C.F.)
5 CBQF—Centro de Biotecnologia e Química Fina—Laboratório Associado, Escola Superior de Biotecnologia, Universidade Católica Portuguesa, 4169-005 Porto, Portugal; aloliveira@porto.ucp.pt
6 Núcleo de Pesquisa e Extensão LACOM, Universidade Federal da Paraíba, João Pessoa PB 58051-085, Brazil; andrel_ltm@hotmail.com (A.L.M.d.O.); mgardennia@quimica.ufpb.br (M.G.d.F.)
* Correspondence: edsonfilho@ufpi.edu.br

Citation: Vieira, E.; Silva, M.; Maia-Filho, A.; Ferreira, D.; Figuerêdo-Silva, J.; Rovaris, K.; Fialho, A.C.; Leite-Oliveira, A.; Menezes de Oliveira, A.L.; da Fonseca, M.G.; et al. Effect of Cerium-Containing Hydroxyapatite in Bone Repair in Female Rats with Osteoporosis Induced by Ovariectomy. *Minerals* **2021**, *11*, 377. https://doi.org/10.3390/min11040377

Academic Editor: Alejandro B. Rodriguez-Navarro

Received: 29 January 2021
Accepted: 30 March 2021
Published: 2 April 2021

Abstract: Osteoporosis is a public health problem, with bone loss being the main consequence. Hydroxyapatite (HA) has been largely used as a bioceramic to stimulate bone growth. In our work, a cerium-containing HA (Ce-HA) has been proposed and its effects on the antimicrobial and bone-inducing properties were investigated. The synthesis of the materials occurred by the suspension–precipitation method (SPM). The XRD (X-ray Diffraction) confirmed the crystalline phase, and the Rietveld refinement confirmed the crystallization of HA and Ce-HA in a hexagonal crystal structure in agreement with ICSD n° 26205. Characterizations by FT-IR (Fourier Transform Infrared Spectroscopy), XPS (X-ray Photoemission Spectroscopy), and FESEM-EDS (Field Emission Scanning Electron Microscope-Energy Dispersive X-ray Spectroscopy) confirmed the presence of cerium (Ce^{3+} and Ce^{4+}). The antibacterial activity of Has was evaluated against *Staphylococcus aureus* 25,923 and *Escherichia coli* 25,922 strains, which revealed that the material has antimicrobial properties and the cytotoxicity assay indicated that Ce-containing HA was classified as non-toxic. The effects of Ce-HA on bone repair, after application in bone defects in the tibia of female rats with osteoporosis induced by ovariectomy (OVX), were evaluated. After 15 and 30 days of implantation, the samples were analyzed by Raman, histology and X-ray microtomography. The results showed that the animals that had the induced bone defects filled with the Ce-HA materials had more expressive bone neoformation than the control group.

Keywords: hydroxyapatite; cerium; ovariectomy; osteoporosis; bone regeneration

1. Introduction

Osteoporosis is an osteometabolic disease related to age and characterized by low bone strength, leading and microstructural deterioration of bone tissue. Therefore, it is a public health problem due to the incidence in the elderly population, mainly affecting women due to menopause [1]. It is believed that on average, 50% of women aged 50 years or older should suffer fractures as a result of osteoporosis throughout life [2].

In view of this situation, several treatment measures are employed to reduce such a problem [3]. Thus, the use of bone grafts has been adopted as a strategy for bone tissue engineering. However, there is a high risk of infection, disease transmission and immune

reaction [4]. The difficulties in using these types of grafts creates the setting for the search for new bioactive materials which, consequently, are receiving increasing attention [5].

Hydroxyapatite (HA), a bioactive bioceramic, biocompatible, biodegradable, non-toxic, osteoconductive, etc., is used in the treatment of bone damage and defects, in particular by contributing to the optimization of implant fixation [6]. It has similarity to the biological apatite present in bones and teeth, may be of natural or synthetic origin, and is characterized by presenting a Ca/P ratio of 1.57 to 1.67, which favors the mechanism of bone growth [7,8].

Therefore, a great advantage of the use of this type of calcium phosphates in the engineering of bone tissue is that it has high biocompatibility with the hard tissues, and there is also biocompatibility with soft tissues such as the gingiva, skin, muscles, the coating of prostheses, cements in dental restoration procedures, etc. [9–11]. Another effective alternative to enhance the biocompatibility of these biomaterials, and consequently, its application in vivo, is the addition of dopants [12,13]. Reger and collaborators have confirmed that the association of certain ions to nano-HA causes non-toxic effects to the material and potentiate activity regarding cell proliferation [14]. A study with Zn shows that its addition in the HA lattice resulted in an increase in cellular metabolism in the medium after 72 h of incubation [15]. Other studies with magnesium, strontium, silver, and gold containing HA have shown satisfactory effects on bone regeneration caused by osteoporosis in animal models [16–18]. For example, Hu et al. [19] suggest that the cerium participates in regulating the migration and osteogenic differentiation of bone marrow stromal cells (BMSCs). An in vitro study of some biological properties, such as the hemocompatibility, antibacterial activity and biocompatibility of ion-containing HA with different concentrations of cerium (IV) (0.5% to 1.25%) demonstrated the biocompatible nature of the material with human blood (5% hemolytic ratio) and excellent efficiency of the inhibition of pathogens for *Escherichia coli*, *Pseudomonas aeruginosa*, *Staphylococcus aureus*, and *Bacillus subtilis* [20]. In vitro and in vivo studies indicate that there are other positive responses of the organisms to cerium, such as osteoblast proliferation, differentiation and mineralization [21], and as a neuroprotective agent [22,23]. Finally, Phatai et al. [24] synthesized Ce-containing HA nanoparticles by an ultrasonic-assisted sol-gel technique. Ce concentration varied from 0.5% to 2.0 wt% and characterization showed that the Ce ions incorporated into the HA lattice. The presence of the cerium ion in two oxidation states (Ce^{3+} and Ce^{4+}) was also observed.

Accordingly, the present work aims to synthesize and characterize the cerium-containing hydroxyapatite (Ce-HA) particles (containing 5.00 mol% Ce) (we chose this concentration based on previous studies in our laboratory), in addition to studying its antibacterial properties against the inhibition of growth of two strains of bacteria (Gram-positive and Gram-negative), as well as to investigate its potential effect on cell viability in vitro (MTT assay). Moreover, an in vivo study was conducted to evaluate the bone repair properties of Ce-HA in rats with ovariectomy-induced osteoporosis (OVX).

2. Materials and Methods

2.1. Chemicals

For the synthesis of HA and Ce-HA, the following reagents were used: calcium hydroxide (Vetec, Odense, Denmark), $Ca(OH)_2$; dibasic ammonium phosphate (Neon), ($(NH_4)_2HPO_4$) and cerium nitrate ($Ce(NO_3)_3$), (Sigma–Aldrich, St. Louis, MO, USA). The reagents had not undergone previous purification processes and the water used for the synthesis processes was obtained by purification in a Milli-Q® system (Millipore Corporation, Burlington, MA, USA).

2.2. Synthesis of Hydroxyapatite and Ce-Hydroxyapatite

The synthesis of HA was performed by the suspension–precipitation method (SPM) [25], using $Ca(OH)_2$ and $(NH_4)_2HPO_4$ as precursor reagents in the stoichiometrically determined amounts according to molar ratio of Ca/P (Equation (1)). The $Ca(OH)_2$ and $(NH_4)_2HPO_4$

were dissolved in 100 mL of water. The synthesis was carried out at room temperature under stirring for approximately 3 h in basic pH (pH ~ 10–11) and the synthesis occurred with no need for pH adjustment. The resulting colloidal dispersions were centrifuged, washed with deionized water and the product was dried in the oven at 110 °C for about 12 h. The synthesis of Ce-HA was also performed by the SPM synthetic route, using the same procedure adopted for the synthesis of HA. However, at this stage, the addition of the cerium dopant (xmolsCe = 5.00 % mol or 0.050 mol) occurred in proportion to the percentage of calcium of hydroxyapatite ($Ca_{10-x}Ce_x(PO_4)_6(OH)_2$) (Equation (2)) [26]. The synthesis procedure of Ce-HA occurred with the simultaneous addition of $Ca(OH)_2$, $(NH4)_2HPO_4$, and $Ce(NO_3)_3$ dissolved in 100 mL of deionized water, also at room temperature under magnetic stirring for about 3 h at basic pH (pH 10–11). The obtained powders were milled with the aid of the mortar and pestle and passed in a 35 VT sieve with an aperture of 425 μm.

$$10Ca(OH)_{2(s)} + 6(NH_4)_2HPO_{4(s)} \rightarrow Ca_{10}(PO_4)_6(OH)_{2(s)} + 12NH_{3(g)} + 18H_2O_{(l)} \quad (1)$$

$$Ca(OH)_{2(s)} + 0.05Ce(NO_3)_{3(aq)} + 6(NH_4)_2HPO_{4(s)} \rightarrow Ca_{9.95}Ce_{0.05}(PO_4)_6(OH)_2\downarrow + 18H_2O_{(l)} + 12NH_{3(g)} \quad (2)$$

2.3. Characterization

The synthesized powders were characterized by X-ray diffraction (XRD). The diffractograms were collected from 5° to 75° at 2θ with a scan rate of 2°/min and a data collection time of 40 min. Monochromatic Cu–Kα radiation (λ = 1.5406 Å) was used on a LABX–XDR 600 by Shimadzu (Kyoto, Japan). The obtained diffractograms were compared with profiles reported in the literature and database cards (ICDD and ICSD). The average crystallite size was estimated using the Debye–Scherrer equation (the crystalline plane used was (002) [27]. Phase composition identification was performed by Rietveld method using GSAS EXPGUI 2012 software (2.0 version, Los Alamos, NM, USA). For the Rietveld refinement analysis, XRD data were collected in the 2θ range from 10° to 110° with a scanning rate of 0.02°/min and exposure time of 90 min. Calibration of the X-ray diffractometer was performed prior to XRD pattern acquisition. The NIST standard reference material LaB_6 (NIST-600b) was used in this calibration. The collected XRD pattern of the reference material was then used to obtain the initial input parameters for all the refinements. In addition, the crystallographic information on the ICSD card n° 26,205 for pure HA was employed as the initial structural refinement model. Fourier-transform infrared spectroscopy (FTIR) spectra were obtained using a Vertex 70 spectrophotometer (Brucker Optics, Billerica, MA, USA). The KBr pellet method was used which required 32 sweeps in the region of 4000 to 400 cm^{-1} with a resolution of 4 cm^{-1}. The morphological analyses of the synthesized materials were investigated using a field emission scanning electron microscope (FESEM) (QUANTA 250 FEI, FEI Company, Eindhoven, The Netherlands). Elemental analysis by energy dispersive spectroscopy (EDS) was performed using an Apollo X EDAX (FEI Company, Eindhoven, The Netherlands) probe attached to an FESEM. The X-ray photoemission spectra (XPS) were obtained using a spectrometer system (ESCA+, Scienta-Omicron, Taunusstein, Germany) equipped with a hemispherical analyzer (EA125) and a monochromatic Al Kα X-ray source (Xm 1000, 1486.7 eV). The X-ray source was used with a power of 280 W, as the spectrometer worked in a constant pass energy mode of 50 eV.

2.4. Antibacterial Activity by Direct Contact

Antibacterial activity was performed using Gram-positive (*S. aureus*) (ATCC 25,923) and Gram-negative strains (*E. coli*) (ATCC 25,922) by the direct contact technique (DCT). Cultures were obtained by transferring bacteria on nutrient agar into a falcon tube containing 3.0 mL of brain heart infusion (BHI) medium, followed by incubation at 37 °C for 24 h. From this BHI culture, a standardized bacterial suspension was prepared at a density equivalent to 0.5 on the McFarland scale, or approximately 1.5×10^8 CFU/mL. Serial decimal dilutions were then performed in physiological saline solution, obtaining

a suspension of 1.5×10^4 CFU/mL for both bacteria. The antimicrobial test was performed by direct contact, according to the methodology of Zheng and Zhu (2003) [28], resulting in the counting of colony-forming units (CFUs). For the test, the standardized bacterial suspension was submitted to decimal serial dilutions until the 10^{-4} dilution (1.5×10^4 CFU/mL) was obtained, upon which 2000 µL of this diluted suspension was transferred to a sterile falcon-type tube. Next, 2000 µg of the HA and Ce-HA was added to determine the inhibitory effect and 100 µL of this suspension were transferred to Petri dishes containing the nutrient agar medium. Petri dishes were then seeded with the aid of a Drigalski loop by the spread plate method and were incubated at 37 °C for 24 h. Then, the counting of colony-forming units (CFUs) was performed. The inhibitory effect by each test solution was calculated according to the Equation (3):

$$\eta = (N_1 - N_2)/N_1 \quad (3)$$

where η is defined as the inhibitory effect, N_1 is the arithmetic mean of the colony-forming units of the control plates, N_2 is the average of the colony-forming units of each of the solutions tested and the results set out in percentages. As the positive control, nutrient agar plates containing bacterial suspension and saline solution (2000 µL) were used, as well as plaques containing the bacterial suspension. All tests were performed in triplicate.

2.5. Cytotoxicity Assay

The in vitro cytotoxicity assay was performed in accordance with standard procedures (ISO 10993-5:2009). Cell viability was analyzed by MTT (3(4,5-dimethylthiazol-2-yl)-2,5-diphenyltetrazoliumbromide) colorimetric assay. Human fibroblast cells (GM07492) were initially seeded (15×10^3 cells/well) in 96-well culture dishes and maintained in Dulbecco's modified eagle's medium (DMEM) enriched with fetal bovine serum (FBS-10% v/v) and antibiotics (penicillin and streptomycin). Cells were then incubated (Panasonic-CO_2 incubator MOC-19 AIC-UV, Osaka, Japan) at a humidified atmosphere containing 5% CO_2 and 95% atmospheric air for cell adhesion. Simultaneously, samples were weighed, sterilized, immersed and extracted in a culture medium (20 mg/mL, HA powders/DMEM free of bovine fetal serum) at 37 °C for 24 h and the extracts were collected for the cytotoxicity assay [29]. After that, the culture medium of the seeded wells was replaced by 100 µL of medium resulting from the extraction procedure of each sample. This experiment was carried out in triplicate and maintained under standard culture conditions for 24 h. Subsequently, culture medium was removed from the wells, which were washed with phosphate buffered saline (PBS 2×). Aliquots of 50 µL of MTT were added to each well and the cells were kept in culture conditions for 4 h. After this period, they were added by 100 µL of isopropyl alcohol and the well content was mechanically homogenized until complete formazan solubilization. The absorbance optical density values of samples (OD) were obtained using a spectrophotometer at 570 nm wavelength. The cytotoxic effect was expressed in percentage using the following equation, where control group considered as 100% cell viability (Equation (4)) [15]:

$$\mathrm{OD}(\%) = \left(\frac{\text{Absorbance of treated cells}}{\text{Absorbance of controlled cells}} \right) \times 100 \quad (4)$$

The OD value of each sample was converted into percentages of cell viability in relation to the negative control group (DMEM + 10% FBS = 100% of cell viability). A positive control group was performed (cytotoxic effect reference) by the addition of dimethyl sulfoxide (DMSO 30% v/v) to the culture medium (DMEM + 10% FBS).

2.6. In Vivo Studies

The experimental protocol for the study was approved by the Animal Use Ethics Committee of the State University of Piauí (UESPI) under the terms of Law n°. 11,794/2008,

registered under number 0097/2017 and in accordance with the guidelines of the National Institutes of Health guide.

2.6.1. Surgical Procedure of Ovariectomy (OVX)

Thirty-six female Wistar rats with body weights between 160 and 240 g were used in this study. The rats were kept in a room (T = 25 °C ± 2 °C) with a photoperiod of light and darkness (16 h of light: 8 h of dark), in polypropylene boxes (4 animals/box) with food and water ad libitum. The animals received cutaneous atropine, at the dose of 0.04 mL/100 g, 20 min after the anesthetic procedure. Subsequently, the rats were anesthetized with a combination of ketamine (80 mg/kg) and xylazine (10 mg/kg), intraperitoneally. Then, the ovariectomy (OVX) was performed according to the methodology described by Khajuria and collaborators [30]. The sterilization of the powders was performed in autoclave at 121 °C for 30 min.

2.6.2. Bone Defect Procedure

After 60 days of OVX, surgical procedures were performed to create bone defects in the tibia of the animals. A surgical drill (n = 8) was used to perform the bone defects. Bone defects were performed in the lateral portion of the tibia of each animal, monocortical with a diameter of 2 mm and depth until reaching the medullary canal. The amount of hydroxyapatite particles added on the bone defect was approximately 0.01 g. After the surgical procedure, analgesic therapy with tramadol at a dose of 0.02 mL/100 g intramuscularly during the first 24 h postoperatively was performed every 6 h. Ambient temperature was controlled, the rats were kept in the vivarium during the experimental periods, with feed and water ad libitum, and were observed periodically to check for behavioral and systemic abnormalities. The female rats were distributed in 4 groups with 9 animals, in two postoperative times of 15 and 30 days. Four groups were formed for in vivo study: sham control or sham-operated control group (SC), where ovariectomy was simulated, clot control (CC), in rats that underwent ovariectomy, the defect being filled by clot without any treatment and, finally, the third group that had the defects filled with the Ce-HA bioceramic powder; this group was named Ce-HA-OVX. The BONE group was used as a reference control.

2.6.3. Tissue Processing

At the end of each experimental period, 15 and 30 days for each group, the animals were euthanized according to the appropriate ethical principles (COBEA) for the dissection of the samples that were submitted to the analysis. Euthanasia was performed with an overdose of the anesthetic combination of xylazine (10 mg/kg) and ketamine (80 mg/kg) prepared in the same syringe and given intramuscularly deep. After latency and immediately after cardiorespiratory arrest, the bone pieces with areas of interest were removed and fixed in 10% v/v neutral formol (pH = 7.0) solution, washed and decalcified in 30% v/v formic acid solution. Then, they were placed in nitrogen gas for further analysis.

2.7. Calcium Dosage

Before euthanasia, blood samples were collected from Wistar rats randomly (2 rats/group). The collected blood samples were centrifuged at 3500 rpm for 5 min and the serum was separated for calcium dosing.

2.8. Confocal Raman Spectroscopy

The spectra were obtained using the Senterra Confocal Raman (Bruker, Billerica, MA, USA) microscope, equipped with a charge-coupled device as a detector (CCD). For excitation, the spectrometer used a laser with a wavelength of 785 nm with a 40× lens for observation of samples. The Raman signal was collected by a CCD and recorded on a computer connected to the system. The output power was 20 mW with two integrations of 10 s each (approximately 20 s/spectrum). To eliminate sample fluorescence, a fourth

order polynomial was performed for each spectrum in the regions of 900–1200 cm^{-1} and 2700–3500 cm^{-1}. This procedure was performed using PeakFit to characterize changes in mineral components of the newly formed bone [31]. Lastly, the crystallinity indices of bone mineral were obtained through the profile of the highest intensity band, 960 cm^{-1}, referring to the symmetrical stretching vibration of the PO_4^{3-} group of phosphate.

2.9. Histological Examination of Repair Tissue

Specimens of the tibia, including the area corresponding to the bone defect, were fixed in 10% *v*/*v* neutral buffered formalin (24 h, pH = 7.0) and decalcified in 10% EDTA (Ethylenediaminetetraacetic acid) for 2 weeks. After the decalcification, the specimens were submitted to routine histological processing. The bone defect repair samples were histological analyzed by hematoxylin-eosin (H.E.) staining. The histological analysis was performed according to the methodology described by Ding and collaborators [32].

2.10. Micro-Computational Tomography (Micro-CT)

Areas of interest of the tibiae with the defects were scanned by X-ray micro-computed tomography (micro-CT) (μCT-SkyScan 1172, Bruker, Billerica, MA, USA). The following parameters were used: 80 kV, 120 μmA, 14 μm, filter of 0.5 mm Al, 0.3 rotation step and 3 frames. In order to reconstruct the volumes, the software NRecon was used with the following artifact corrections: smoothing set at 2, reduction of artifacts into rings set at 5 and reduction by 20% of the beam hardening phenomenon. The generated images were rebuilt in the software Dataviewer (μCT-SkyScan 1172 enabling the visualization in standard position (axial) of all the defects. To analyze the parameters of bone quality, CTAn (μCT-SkyScan 1172) was used; the region of interest analyzed resulted in a disc shaped structure, with a 2 mm diameter and 50 axial vertical cuts. Through the software CTVox (μCT-SkyScan 1172) the tridimensional images were generated and edited.

2.11. Histological Examination of Repair Tissue

The data were statistically analyzed using the GraphPad Prism software version 5.0 (GraphPad Software, La Jolla, CA, USA). The groups were compared using one-way ANOVA applying a post hoc Fisher's test (level significance at a 95% CI, $p \leq 0.05$ was considered for all tests).

3. Results

3.1. Characterization

For the effective confirmation of the phase and assessment of the crystallinity of the material, XRD analysis was performed on the HA and Ce-HA samples. The X-ray diffraction patterns show that the materials are crystalline with no intermediate phases, as presented in Figure 1. The XRD results also revealed the formation of materials with lower crystallinity for synthesis performed without heat treatment. The diffractograms were aligned in X'Pert HighScore Plus software (3.0.5 version, Malver Panalytical, Malver, Worcestershire, UK) by adjusting the peak heights and position. The XRD patterns of the synthesized powders (HA and Ce-HA) show the characteristic diffraction peaks of hydroxyapatite, being indexed according to the ICDD-PDF card 00-001-1008. Among the crystalline planes, (1 1 1), (0 0 2), (1 0 2), (2 1 0), (2 1 1), (2 0 2), (3 1 0), (3 1 2), (2 0 3), (2 1 3) and (5 1 1) were observed at 2θ angles of 26.06°; 28.32°; 32.20°; 34.35°; 39.99°; 46.95°; 49.80° and 53.39°, respectively [33]. The values of the average size of the crystals, which were calculated by the Debye–Scherrer, were 25.87 nm for HA and 34.51 nm for Ce-HA, which might be due to the formation of Ce_2O_3 phase and also to Ce-doping in the HA lattice.

The Rietveld refinement was used to estimate the approximation of the XDR patterns of the synthesized powders in comparison with the structural model of the Crystallographic Information File (CIF) available in crystallographic databases for HA. In addition, an important aspect regarding the quality of the samples (crystalline phase fraction) and the effect of cerium on the structure of the material was investigated by this analysis. Figure 1b

shows the representation of the unit cell structure of the hydroxyapatite simulated by the VESTA (Visualization for Electronic and Structural Analysis) program [34], version 3.4.4 (Koichi MOMMA, Tsukuba, Japan) for Windows that was proposed based on the network parameters (a, b, c, α, β, and γ) and atomic positions (x, y and z) obtained after Rietveld refinement.

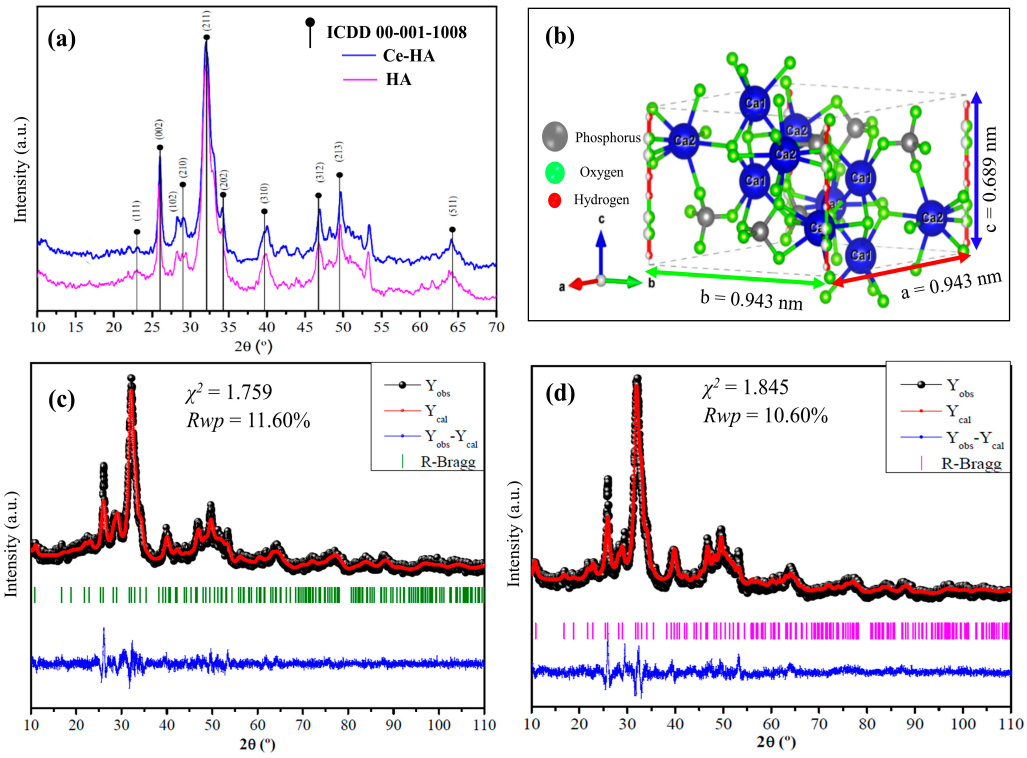

Figure 1. XRD pattern for the (**a**) hydroxyapatite (HA) and cerium-containing HA (Ce-HA) powders synthesized by the suspension–precipitation method (SPM). (**b**) Representation of the unit cells of the hydroxyapatite obtained in this study. Rietveld refinement profiles from XRD data for (**c**) HA and (**d**) Ce-HA.

The calculated patterns are adjusted to the observed experimental pattern, providing the structural parameters of the desired material and its diffraction profile. The observed and calculated XRD profiles of HA powder, as well as the difference between both profiles ($Y_{Obs} - Y_{Cal}$) are shown in Figure 1c,d. All diffraction peaks were perfectly indexed to ICSD card n° 26,205 (hexagonal lattice system and space group P63/m) and the refined lattice parameters were: $a = b = 0.944$ nm and $c = 0.689$ nm for HA. It is important to mention that no secondary phase was observed in the diffractogram of HA.

Ordinarily, Rietveld refinement is qualified as satisfactory as to the empirically obtained value of χ^2 (chi square or goodness of fit: $\chi^2 = R_{wp}/R_{exp}$). Hence, values equal to 2.00 or less are satisfactory [35]. Cavalcante et al. [36] report that the acceptable R_{wp} values are: $R_{wp} < 8\%$—cubic structure (high symmetry and few diffraction peaks); $R_{wp} < 10\%$—medium complex phases (tetragonal, orthorhombic, rhombohedral, and hexagonal) and $R_{wp} < 15\%$—high complex phases (monoclinic and triclinic). R_{wp} calculated for the HA and Ce-HA powders were 10.60% and 10.17%, and the obtained χ^2 values were relatively low: 1.845 for HA and 1.759 for Ce-HA, respectively. Therefore, the values calculated are considered as acceptable according to the basic principle of goodness of fit. Comparative results between the lattice parameters and unit cell volume obtained in this work with those published in the literature are shown in Table 1. Finally, the Rietveld refinement from the Ce-HA XRD datum showed that the material preserved the hexagonal-type HA structure, with smaller lattice parameters ($a = b = 0.942$ nm and $c = 0.675$ nm) when compared to the pure HA synthesized in this work. However, the Ce_2O_3 intermediate phase was evidenced,

and the valuation of the sample composition revealed that 3.02% of Ce is present in the Ce-HA material. As 5%mol of Ce precursor was used in the synthesis, we believe that the additional amount of Ce might be incorporated on the HA matrix as an oxide-type phase (CeO_2 and/or Ce_2O_3), even though the oxide was identified in the refinements. According to the literature, doping HA with Ce^{4+} cations leads to a decrease in the lattice parameters [37]. This behavior might be related to the mismatch between the ionic radii of Ce^{4+} (0.097 nm) and Ce^{3+} (0.114 nm) in comparison to Ca^{2+} (0.106 nm). In addition, Ca/Ce substitution can also implicate the formation of different ionic defects in the HA lattice, which can result in the change of the lattice parameters and unit cell volume, as observed (Table 1). Although the refinements suggest Ce-doping, the formation of Ce_2O_3 (trigonal symmetry and space group P321) or CeO_2 (cubic symmetry and space group F3m3) is not ruled out. The difficulty in determining the precise amount of Ce in Ce-HA is due to the lower crystallinity of the sample obtained in this work.

In order to corroborate the obtained refinement results, the identification of cerium in the hydroxyapatite lattice was performed by EDS, FT-IR, and XPS (Figure 2). By means of the EDS (Figure 2a,b), it was possible to calculate the semi-quantitative Ca/P ratio. The results (Table 2) showed that the Ca/P ratio for HA and Ce-HA ((Ca + Ce)/P) were 1.56 and 1.51, respectively. The values obtained in this work revealed that the hydroxyapatite synthesized is of the calcium deficient type (CDHA or Ca-def HA). Calcium-deficient hydroxyapatite type (CDHA or Ca-def HA) has a Ca/P ratio between 1.50 to 1.67 [24].

Table 1. Comparative results between the lattice parameters and unit cell volume of HA in Ce-HA obtained in this work with those published in the literature.

Hydroxyapatite	Lattice Parameters							Reference
	a (Å)	*b* (Å)	*c* (Å)	*α* (°)	*β* (°)	*γ* (°)	V (Å^3)	
HA	9.439(3)	9.439(3)	6.894(2)	90	90	120	532.01(19)	This study
Ce-HA	9.424(2)	9.424(2)	6.876(2)	90	90	120	528.81(25)	This study
HA	9.424	9.424	6.879	90	90	120	529.09	ICSD 26205
HA	9.418	9.418	6.884	90	90	120	-	[38]
HA	9.418	9.418	6.884	90	90	120	-	[39]
Ce-HA	9.413	9.413	6.873	90	90	120	525.59	[40]
Sr-HA	9.454	9.454	6.911	90	90	120	534.68	[41]

Refined lattice parameters (*a*, *b*, and *c* = axial lengths; *α*, *β*, and *γ* = angles), V = unit cell volume, ICSD = Inorganic Crystal Structure Data.

FESEM showed the formation of non-uniform particle clusters with irregular surface for HA (Figure 2c). The cerium-containing hydroxyapatite sample (Figure 2d) also shows the formation of non-regular particle agglomerates. Therefore, the morphology of the material was not altered with the addition of cerium [42].

Table 2. Semi-quantitative Ca/P ratio of HA and Ce-HA obtained by EDS compared to Ca/P ratios available in the literature.

Hydroxyapatite	Ca/P	(Ca + Dop)/P	Analysis	References
HA	1.56	-	EDS	This study
Ce-HA	-	1.51	EDS	This study
Ma-Ca-def HA	-	1.46	EDS	[43]
Ce-HA	-	1.55	EDS	[44]
Zn-HA	-	1.34	EDS	[45]
Bi-HA	-	1.67	EDS	[46]

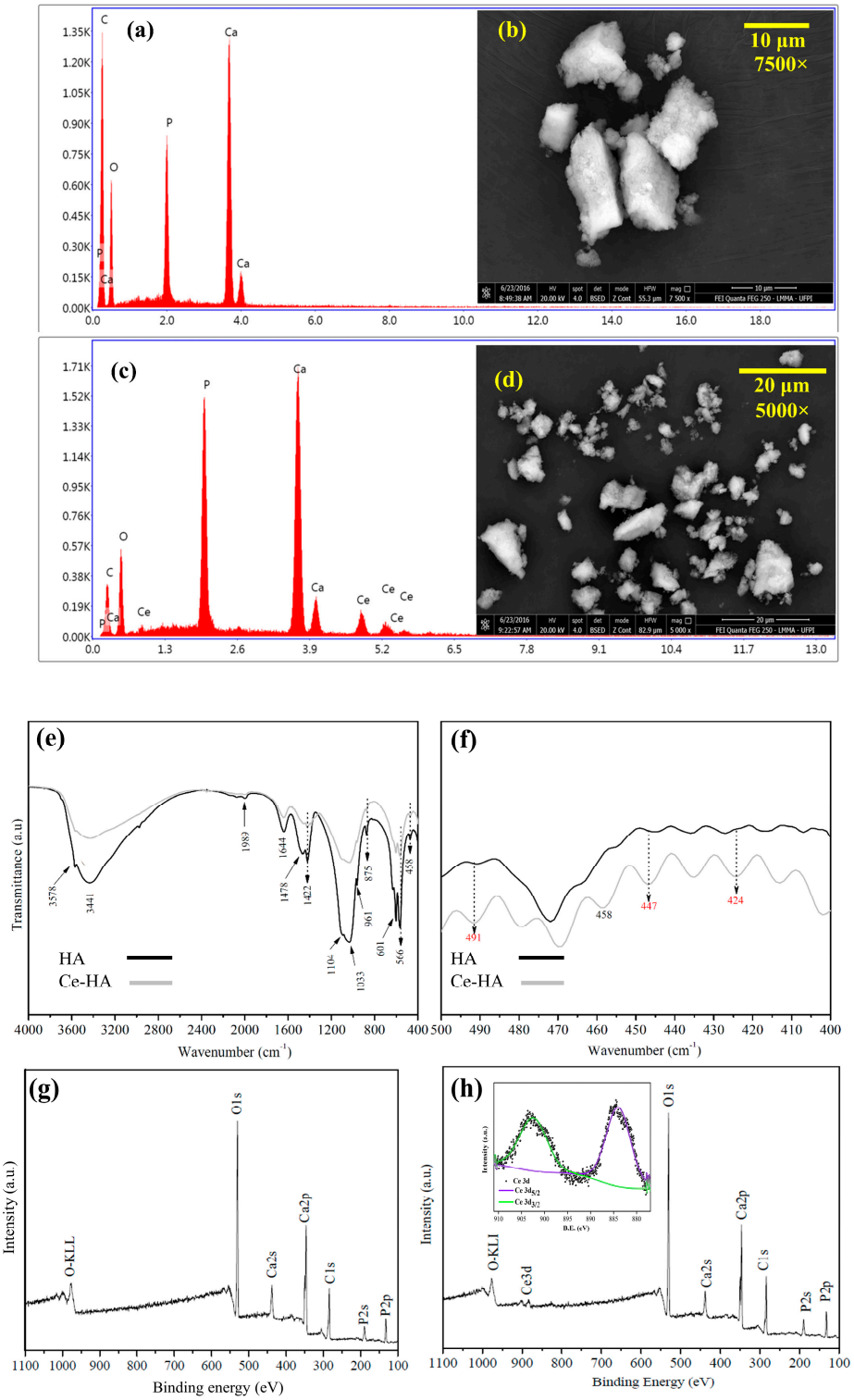

Figure 2. EDS analysis of (**a**) HA and (**b**) Ce-HA, FESEM micrographs of (**c**) HA and (**d**) Ce-HA, FTIR spectra of (**e**) HA and Ce-HA and spectra in the region between 500–400 cm^{-1} for (**e**) HA and (**f**) Ce-HA, (**g**) X-ray photoemission spectra of (**g**) HA and (**h**) Ce-HA.

There is the presence of bands at 1989 cm^{-1}, 1478 cm^{-1}, 1422 cm^{-1}, and 875 cm^{-1} assigned to the CO_3^{2-} deformation and stretching vibrations, which might be due to the carbonation process that promotes the formation of carbonates on the material surface [47]. The carbonate would originate from the CO_2 present in the synthesis carried out outdoors, as well as basic pH (10–11) of the reaction medium ($CO_2 + 2OH^- \rightarrow CO_3^{2-} + H_2O$). The

presence of carbonate is not a setback [47]. Generally, the metal/metal oxides give the FT-IR bands a lower wave number ranging from 400 to 800 cm^{-1} [48,49]. The bands at 491, 458, 447 and 424 cm^{-1} are ascribed to the formation of Ce-O bonds, which are in the IR range of crystalline cerium oxide active phonon modes. These results corroborate the statements generated after refinement cycle.

Chemical composition of the surface of the samples and the chemical state of cerium in Ce-HA were confirmed by X-ray photoelectron spectroscopy (XPS, Figure 2g,h). Peaks at binding energy (B.E.) of 439.74 eV (Ca 2s), 347.54 eV (Ca 2p), 187.73 eV (P 2s), 131.78 eV (P 2p) and 529.27 eV (O 1s) were detected, revealing the presence of the elements Ca, P and O that chemically compose the hydroxyapatite in both HA and Ce-HA samples. In addition, the presence of the photoemission signal of Ce 3d in the XPS survey spectrum of Ce-HA, confirm that the desired sample was obtained. According to the literature, Ce 3d XPS spectrum is quite complex and more complicated than other materials due to hybridization between Ce 4f and O 2p levels [50]. In Ce 3d XPS spectrum for Ce(IV), six well-defined peaks, which are associated to $3d_{5/2}$ and $3d_{3/2}$ doublets, are expected. For Ce(III) species, four visible components is observed in XPS. In respect of the coexistence of mixed Ce(IV) and Ce(III) cations, a XPS spectral broadening is observed. Based on this, the deconvolution procedure was performed in the photoemission line of Ce 3d (Figure 2h, highlighted area in blue) between 880 to 905 eV. From this analysis, only four main peaks corresponding to the pairs of spin–orbit doublets ($3d_{5/2}$ and $3d_{3/2}$) were evidenced. The doublets $3d_{5/2}$ and $3d_{3/2}$ are located at binding energy (B.E.) of 881.82 and 899.36 eV, respectively, and their corresponding strong satellite peaks are observed at 899.36 and 903.31 eV. These peaks are associated to Ce(III) [51,52]. Bêche et al. [53] observed the similar XPS feature in $CePO_4$ material and this agrees with our refinement results that suggested Ce-containing HA formation. In addition, a small peak is observed at 916.42 eV, which is also associated to the $3d_{3/2}$ component of Ce, is the fingerprint of Ce(IV). This peak is observed only in Ce(IV) spectrum, being absent for Ce(III). Table 3 shows the type of spin–orbit components with their corresponding B.E. and chemical composition of the two cerium chemical species.

Table 3. XPS spectrum data for the identified cerium species.

Ce Oxidation Type	B.E. (eV)	Spin–Orbit Component	%Area
(III)	881.82	$3d_{5/2}$	27.00
(III)	885.29	$3d_{5/2}$	24.02
(III)	899.36	$3d_{3/2}$	12.67
(III)	903.31	$3d_{3/2}$	26.87
(IV)	916.42	$3d_{3/2}$	9.44

(IV) = Ce^{4+}, (III) = Ce^{3+} and B.E. = Binding Energy.

The inter-component (spin–orbit coupling) energy separation (ΔE) for the Ce 3d orbitals is: ΔE 17.54 for Ce(III). This value is close to that reported by Bêche et al. (2007) [53] for $CePO_4$, which can suggest that Ce-doping occurred in Ce-HA synthesized in this work. It is worth mentioning.

3.2. Antibacterial Test by Direct Contact and MTT Assay

The antibacterial activities of HA and Ce-HA against *S. aureus* (ATCC 25,923) and *E. coli* (ATCC 25,922) are shown in Figure 3a and the values of the antibacterial activity were calculated using Equation (3). Among the assayed materials, Ce-HA had the highest inhibitory effect for both groups of bacteria. The bacterial growth inhibition results for the Ce-HA, when compared to HA, had an inhibitory increase of about 42.86% for *S. aureus* 41.85% for *E. coli*. Figure 3b shows the photographs of the plates with the results obtained for the growth of the colonies.

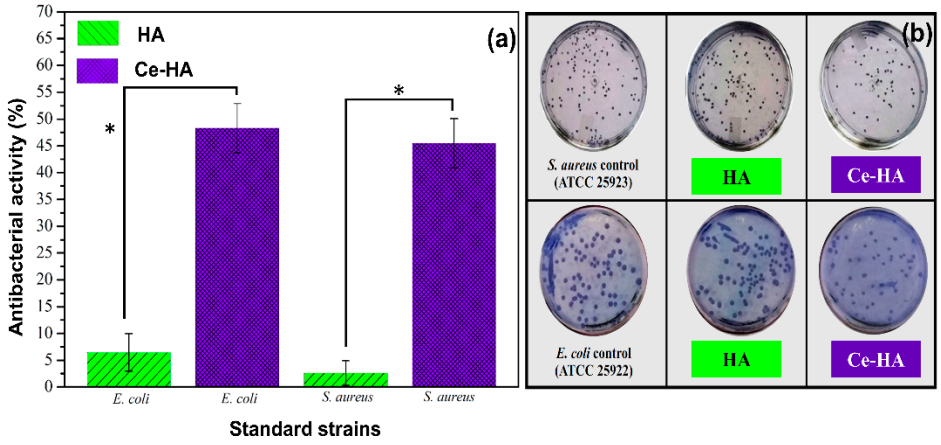

Figure 3. (**a**) Inhibitory effect of Ce-HA on standard strains of *E. coli* (ATCC 25,922) and *S. aureus* (ATCC 25,923) and (**b**) inhibitory effect by direct contact with HA and Ce-HA. Statistical analysis: one-way ANOVA applying a post hoc Fisher's test * $p \leq 0.05$.

Cytotoxicity for the HA and Ce-HA was investigated by the MTT assay on human fibroblast cells (GM07492). The results showed (Figure 4) that none of the tested samples had viability levels compatible with a cytotoxic effect (cell viability $\leq$ 80%) [54]. Statistical analysis showed that Ce-HA presented cell viability levels (99.1±3.2%) similar to the negative control group (100%) and significantly ($p \leq 0.05$) higher than the HA (89.4 ± 1.0).

Therefore, the synthesized powders (HA and Ce-HA) do not interfere in the cellular metabolic activity and, consequently, in the cellular viability. In other words, the materials are non-cytotoxic (growth inhibition lower than 25%) and can be considered as noncytotoxic. This result is similar to that found in the literature [20] for Ce-containing HA for in vitro tests on cell viability. In view of these findings, the Ce-HA material evaluated in vivo, in rats with osteoporosis induced by ovariectomy.

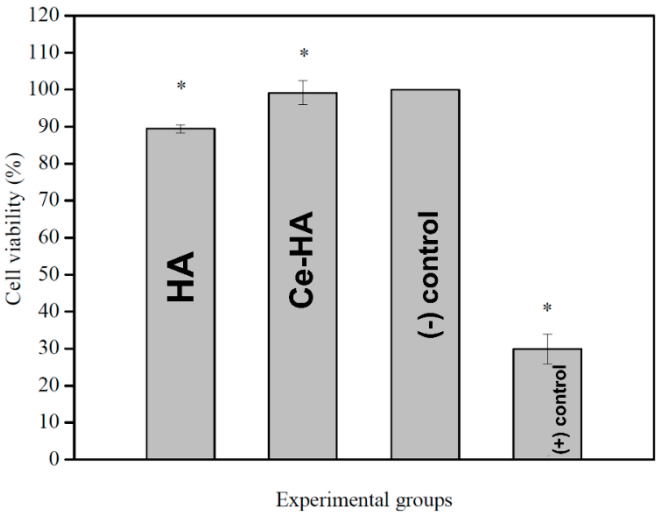

Figure 4. MTT-formazan in vitro assay of HA and Ce-HA performed with human fibroblast cells lineage (GM07492). Results are expressed as a percentage of cell viability relative to the negative control group (DMEM + 10% FBS). The positive control group as cytotoxic effect reference (DMEM + 10% FBS + 30% DMSO). Statistical analysis: one-way ANOVA applying a post hoc Fisher's test * $p \leq 0.05$.

3.3. In Vivo Study

3.3.1. Calcium Dosage

The hematological parameter is shown in Figure 5. This parameter was considered as a reference for the evaluation of the results of the experimental procedures of this work. The adoption of such a measure is due to the literature presenting disagreements between the values obtained for hematological and biochemical parameters.

Accordingly, the relevance of establishing benchmarks for each animal house or laboratory is relevant [55], thus it was possible to evaluate by the calcium dosage that the Wistar rats submitted to OVX showed a significant reduction in the amount of calcium when compared with the positive control. Most of the calcium is present in the bone tissue, therefore, it is evident that the decrease in the amount of calcium suggests a loss of bone mass, and consequently, an alteration in the bone microarchitecture, making the bone tissue more brittle and more susceptible to fractures.

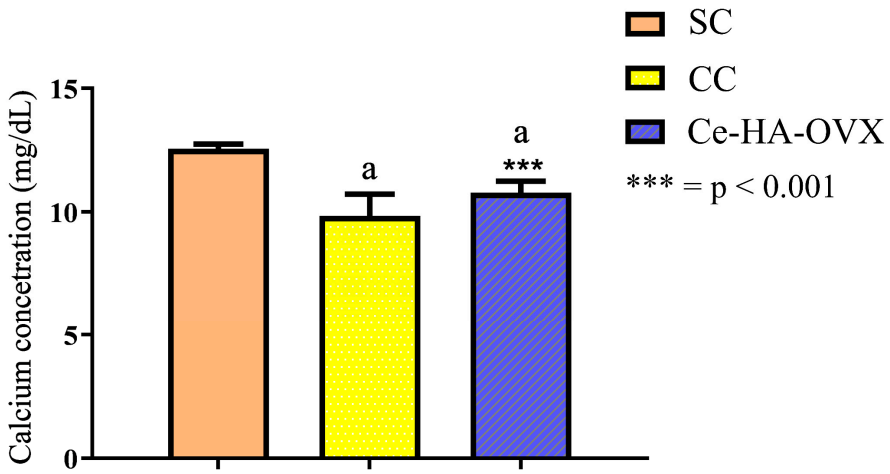

Figure 5. Dosage of calcium concentration for Wistar rats who underwent the ovariectomy process. SC: sham control, CC: clot control and Ce-HA-OVX: group that received the Ce-HA implant, a: $p < 0.05$ when compared to CC and Ce-HA-OVX groups.

3.3.2. Raman Spectroscopy of Bone Tissue

Raman spectroscopy analysis was used to evaluate the bone mineral content in the bone defect area, since this analysis is more specific in identifying the chemical composition of hydroxyapatite [56]. Figure 6 shows the Raman spectrums obtained from the cortical region of the bone tissue of the three groups evaluated in this study (SC, GC and Ce-HA-OVX), after euthanasia in the period of 15 and 30 days (Figure 6a–c).

The Raman band at 960 cm^{-1} (ν_1 PO_4^{3-}) was used to obtain the integrated area of the spectrum. The spectra (Figure 6a,c) show that the groups have the same peak positions, but with different intensities. Ce-HA-OVX (Figure 6c) shows a higher peak intensity compared to other groups evaluated for both time periods. The Raman band of the BONE group was used as a reference. This area is strictly linked to the amount of hydroxyapatite in the neoformed bone, meaning that the higher the intensity, the greater the phosphate concentration [57]. For each group, the mean peak intensity was calculated.

Statistical analyses of peak phosphate data (960 cm^{-1}) were performed. For 15 day (Figure 6b), the results indicated that there is a more significant area in the CS group in relation to the CC group ($p < 0.05$), but higher phosphate levels were observed in the Ce-HA-OVX group in relation to the SC and CC groups ($p < 0.05$) and statistical differences in the area between the BONE group in relation to the areas of the other groups were observed. After 30 days (Figure 6d), the Ce-HA-OVX group exhibited the same statistical behavior observed over the period of 15 days.

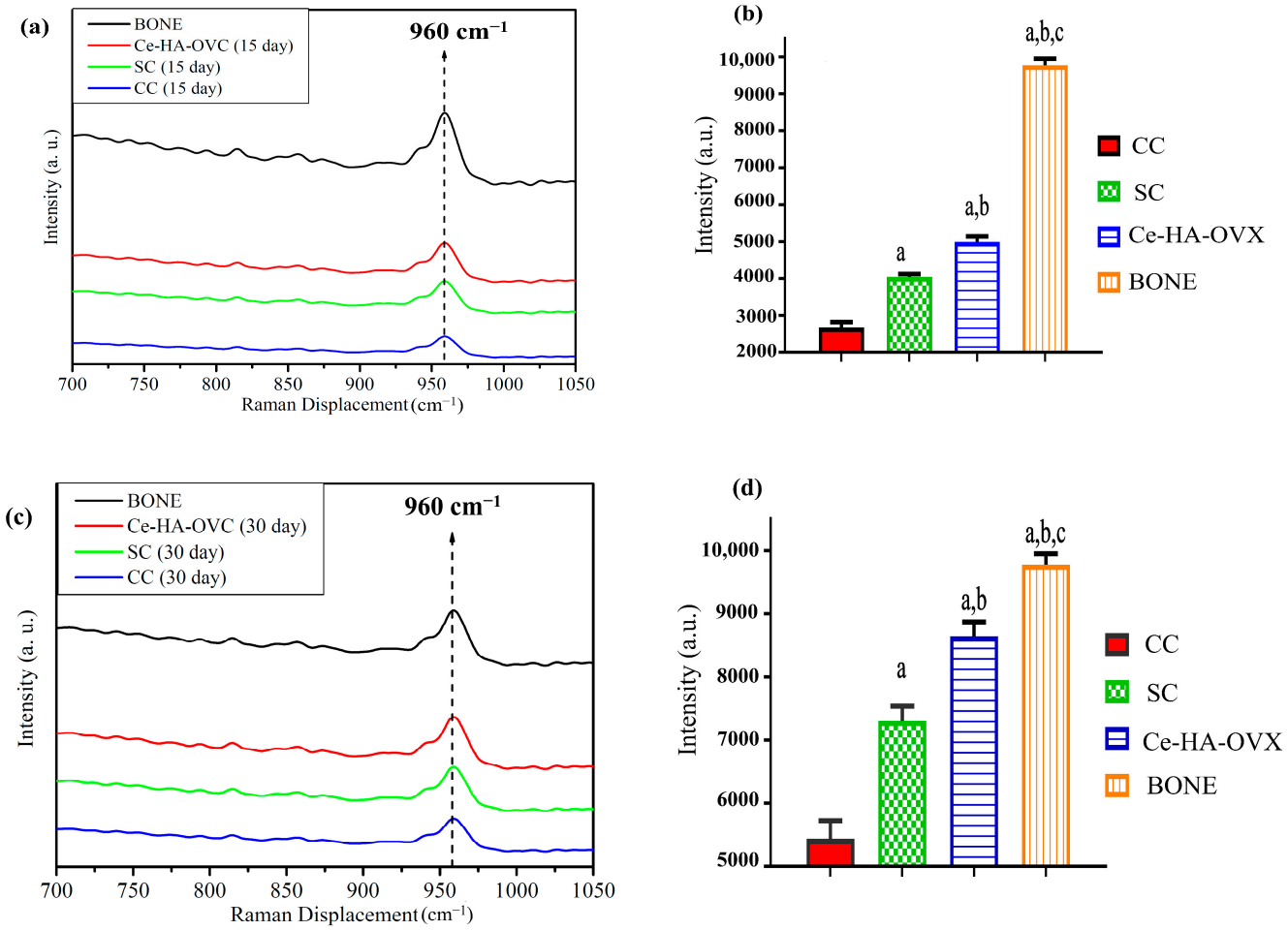

Figure 6. (**a**) Raman spectra and (**b**) statistical analysis for 15 days. (**c**) Raman spectra and (**d**) statistical analysis for 30 days. Caption: BONE = control group reference for the two time periods (a = $p < 0.05$ when compared to the CC group; b = $p < 0.05$ when compared to SHAM group; c = $p < 0.05$ when compared to the Ce-HA-OVX group—Statistical analysis: one-way ANOVA applying a post hoc Fisher's test $p \leq 0.05$).

3.3.3. Histological Analysis

For the 15-day postoperative period, in the SC group, new trabecular bone neoformation was observed filling the bone defect, with a primary or interlaced matrix containing osteoblasts and entrapped osteocytes with their distribution being randomized (Figure 7a). In the CC group, most of the specimens presented bone neoformation with a very immature appearance, with deposition in thin trabeculae and uneven distribution of non-mineralized osteoid material (Figure 7b). The specimens of the Ce-HA-OVX group exhibited intense bone neoformation, of trabecular morphology, with osteoblasts and osteocytes spreading, evidencing better neoformation of the bone tissue with only 15 days when compared to the control groups (Figure 7c). The results for the period of 30 days showed that the SC group presented compact bone neoformation, but not modeled, with primary aspect and containing sparse and spaced osteocytes and osteoblasts, occupying almost all of the area of the defect area in most specimens (Figure 7d). The bone neoformation is compact and thinner in the CC group when compared to the other groups, and still has immature and trabeculated matrix morphology, with only a few osteoblasts filling the entire bone defect. These results were expected, since at this stage there was no filling with any biomaterial in the defective areas, as observed in Figure 7e. Finally, all the specimens of the Ce-HA-OVX group presented bone neoformation, with predominantly compact areas and an unorganized or lamellar matrix containing relatively scarce osteoblasts, occupying the whole area of the defect (Figure 7f).

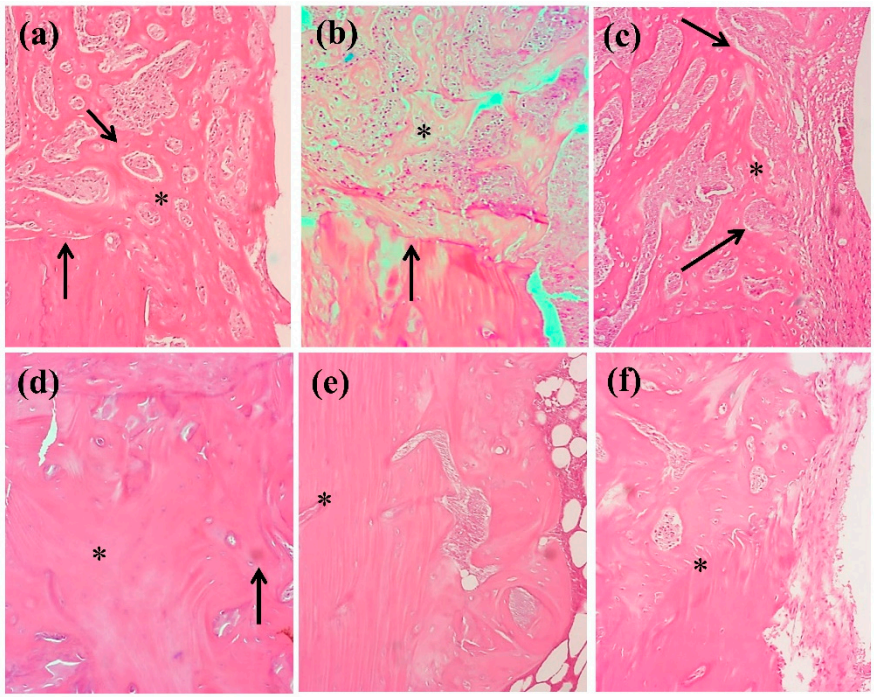

Figure 7. Trabecular bone neoformation (*) with immature aspect, with variable number of osteoblasts and osteocytes (arrows). 15 days: (**a**) = SC group. (**b**) = CC group and (**c**) = Ce-HA-OVX group; 30 days: (**d**) = SC group, (**e**) = CC group and (**f**) = Ce-HA-OVX group.

3.3.4. Micro-CT Analysis

The micro-CT analysis at 15 and 30 days postoperatively is shown in Figure 8. It is possible to observe the reconstruction of the cuts in the CC group, which still has little neoformed bone concentrically disposed from the periphery to the center of the defect (Figure 8a–c). Note the existence of areas with characteristics of bone resorption when compared to the SC group. It is also observed that in the SC group the axial reconstructions present trabecular bone without much density and in less quantity than the Ce-HA-OVX group. The micro-CT still revealed a volume of bone tissue occupying almost the entire defect when compared to the SC group. It was also observed that the trabecular bone permeates the defect in the attempt to repair. The images of the Ce-HA-OVX group (Figure 8a–c) presented atypical bone repair, with trabecular bone denser or initiating maturation and extending to the center of the defect. Remains of the material at the center of the defect were additionally observed, as these are perceived in the 3D images (Figure 8e,f, yellow arrows).

The percentage of BV/TV ratio (bone volume/total volume) (Figure 8b,d) shows statistically no differences related to the volume of neoformed bone tissue between the SC and Ce-HA-OVX groups were observed in the periods of 15 and 30 days. However, when compared to the CC group, all the others are statistically superior. These results fit the purpose of this study, because the CC group underwent the surgical procedure of ovariectomy and the bone defects caused were not filled with Ce-HA, which resulted in a smaller amount of neoformed bone. The B*V*/*V*T ratio still showed that at 30 days, the SC and Ce-HA-OVX groups were statistically superior to the CC group with respect to bone neoformation (Figure 8d).

In the 3D image (Figure 8e,f) it is possible to perceive the formation of new bone tissue (area highlighted in white) for the Ce-HA-OVX group. Thus, it is clear once again that this group presented a volume of bone tissue that occupies almost the entire defect when compared to the SC group. For example, the volume of neoformed bone tissue is higher when compared to the Ce-HA-OVX groups with the CS group. Still, on the reconstruction of the images at 30 days postoperatively, the CC group presents little deposition of bone tissue

when compared to the other groups; this is justified by the occurrence of bone resorption caused by the ovariectomy. These observations occurred for the two time periods under study. The arrows in red (Figure 8e) indicate areas where bone resorption occurred, that is, once again, these results corroborate that the specimens had an induction of osteoporosis. Finally, we noticed a curiosity in one of the specimens studied. It was observed that the spread of Ce-HA occurred outside the area of the bone defect, and this action eventually induced bone growth (bone callus) around other areas (Figure 8f, green area) not studied in this work. This demonstrates that the Ce-HA material has high potential for osteoinduction and bone osteoconduction.

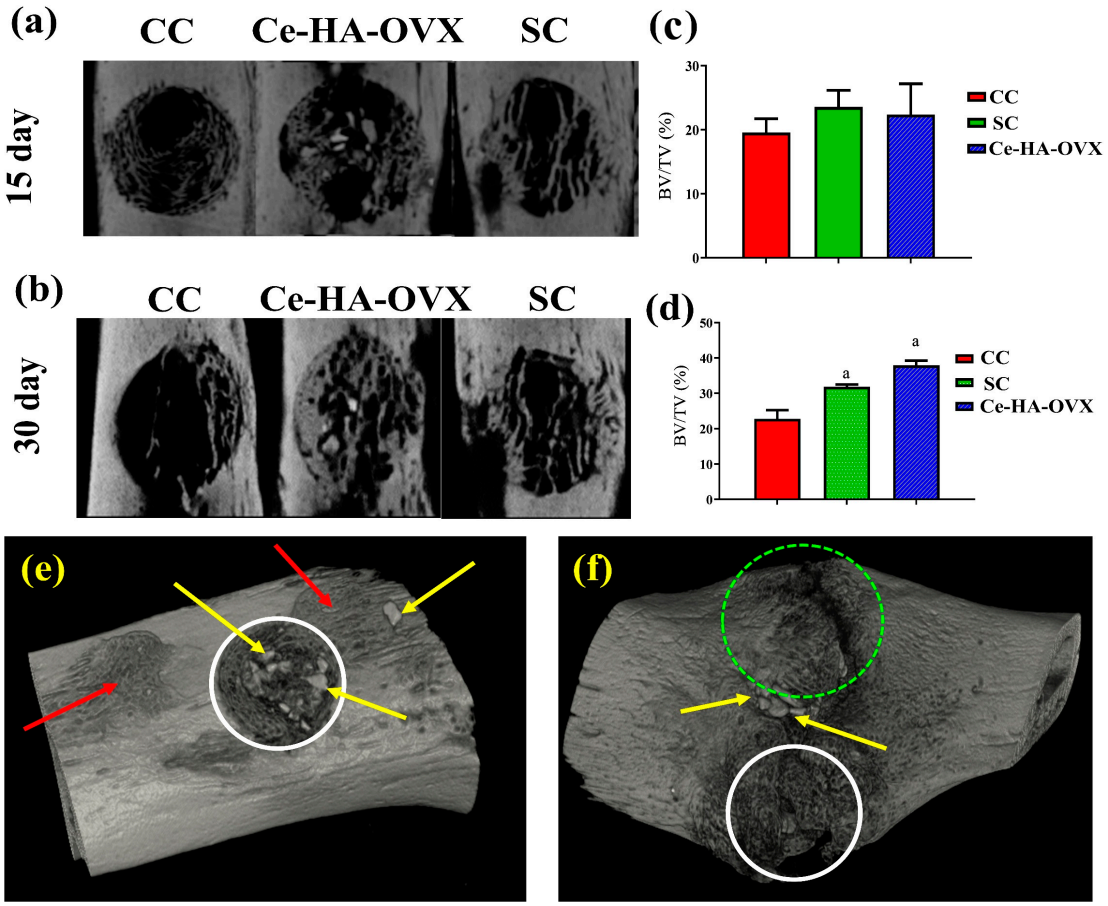

Figure 8. Representative images obtained from Micro-CT of bone neoformation at (**a**) 15 days and (**b**) 30 days postoperatively, statistical analysis of the volume of neoformed bone tissue (BV/TV) after (**c**) 15 days and (**d**) 30 days of implants, (**e**) 3D micro-CT for the Ce-HA-OVX group after 30 days and (**f**) osteoinduction (bone callus) occurred in a specimen after material spreading (a = Statistical analysis: one-way ANOVA applying a post hoc Fisher's test $p \leq 0.05$), (yellow arrows = remains of the Ce-HA, red arrows = bone resorption occurred, area highlighted in white = formation of new bone tissue, and area highlighted in green = bone callus).

4. Discussion

4.1. Characterization

XRD showed that the synthesized materials have good crystallinity, without the presence of intermediate phases. Equations (1) and (2) show the formation mechanism of hydroxyapatite via precipitation synthesis used in the present work. The calculated mean value of the crystallite size was close to that found by de Kaygili et al., 2014 [43]. These authors also calculated the size of the crystals using the (0 0 2) diffraction plane. It is believed that this variation in crystal size observed in the hydroxyapatite synthesized in this study may be a prior indication attributed to the presence of the cerium ion and/or cerium oxide. The hexagonal unit cell of hydroxyapatite consists of 10 calcium ions located

at two distinct sites (Ca1 and Ca2) (Figure 1b). Four Ca1 atoms are located at the ends of a hexagonal unit cell, while the six Ca2 form triangles parallel to the c-axis and located at the corners of the hexagon around the OH^- ion. There are also four distinct oxygen sites (O1, O2, O3 and O4). The O4 is connected to H1 to form the hydroxyl and the sites of P1 are all equivalent, of type $PO_4{}^{3-}$, which are connected to O1, O2 and O3, are the largest ions that construct unit cells, being the only one to determine its structure [58]. Although the amount of ion added was not sufficient to cause the appearance of new diffraction peaks, a variation in lattice parameters and unit cell volume (Table 1), minimally, suggest that there was alteration of the crystal lattice, confirming the results of the XRD. It is also believed that the remaining Ce species added during the synthesis might form a cerium oxide (CeO_2 or Ce_2O_3) layer with low crystallinity on the HA surface, being not identified by Rietveld refinement. A reduction in the unit cell volume of the hexagonal phase was observed after the Rietveld refinement, with the presence of the dopant, when compared with the n° 26205 card (from 529.09 $Å^3$ to 528.55 $Å^3$). This is a strong indication of the possible substitution of Ce^{3+} and Ce^{4+} in the hydroxyapatite lattice. The Ca^{3+} ion (ionic radius = 0.107 nm), because it has a higher ionic radius than the Ca^{2+} ion (ionic radius = 0.100 nm) [59], can replace the calcium of the Ca1 site. While the Ca2 site is occupied by Ce^{4+} ions (ionic radius = 0.097 nm), it has lower ionic radius [40] when compared to the ionic radius Ca^{2+}. This phenomenon has been also evidenced by Phatai et al. [24] by performing Ce L_3-edge XANES in Ce-HA samples. The electronegativity of cerium (1.06) (value close to Ca = 1.01) may be another periodic trend favoring the replacement of calcium by cerium [60]. This high chemical affinity and similarity in its periodic properties suggest that cerium replaces calcium and may thus intervene in the process of bone remodeling. For example, the results obtained by Hu et al. (2014) [19] suggest that cerium promotes the migration and osteogenic differentiation of bone marrow stromal cells.

In relation to the Ca/P ratio, hydroxyapatite (Ca/P = 1.67) is widely used in orthopedic and maxillofacial surgeries to repair bone defects, because it presents excellent osteogenic, osteocondutive and osseointegration properties [60,61]. However, this type of hydroxyapatite is very stable in the body and due to its high crystallinity, a prolonged period for its reabsorption is necessary [62]. In contrast, Ca-def HA is closer than hydroxyapatite to human bone with respect to calcium content and crystallinity [63], besides having a higher rate of dissolution in physiological body fluids. It is also worth noting that natural bone tissues are composed hierarchically by Ca-def HA [64]. Thus, Ca-def HA obtained in this study assumes quite promising properties to have its use turned to medical applications in the field of bone tissue engineering.

The B.E. identified in the XPS revealed the presence of the cerium ion in two oxidation states (Ce^{3+} and Ce^{4+}). The high B.E. relative to the spin–orbit doublets of Ce (IV) presented a percentage area of 9.44%; while for Ce (III), the percentage of area was 90.56%. The thermodynamic properties of cerium, through the Pourbaix Diagram [65], show that the ions are soluble in strong acids, while their hydroxyl complexes are insoluble and quite stable at neutral and basic pH. In addition, cerium ions exhibit a complicated chemistry of solubility due to their high susceptibility to complexation resulting from the influence of electrons on the 4f orbital. This is an important feature of lanthanides, which are known to form hydrated complexes in solution. These complexes are favored due to chemical reactions between anionic ligands with high electronegativity, as is the case of OH^- present in excess in the reaction system [66]. Thus, at basic pH (pH = 10–11), by the Pourbaix diagram, the chemical $Ce(OH)_3$ and CeO_2 are formed. The cerium nitrate used for the synthesis of Ce-HA in this study was $Ce(NO_3)_3$. We believe that the oxidation of dopant (Ce^{3+}) (Equation (5)) has occurred due to synthesis occurring at basic pH and in open system [67].

$$\begin{gathered} Ce^{3+} \rightarrow Ce^{4+} + e^- \\ Ce^{3+} + OH^- + CO_2{}^{3+} \rightarrow Ce(OH)CO_3 \\ 2Ce(OH)CO_3 \rightarrow Ce_2O_3 + H_2O + 2CO_2 \\ 2Ce_2O_3 + O_2 \rightarrow 4CeO_2 \end{gathered} \quad (5)$$

The synthesis by SPM in this study was simple and efficient, once high temperatures were not necessary for the success of the synthesis of Ce-HA. Ciobanu et al. (2015) [39], authors cited in Table 2, synthesized Ce-containing HA in indifferent concentrations (*w*/*w* %) by SPM for antibacterial applications. The (Ca + Ce)/P ratio values range from 1.671 to 1.673 and the synthesis was stirred for approximately 3 h (60 °C). Crystalline HA phases were obtained after calcination for 1 h at 800 °C.

4.2. Antibacterial Test and In Vivo Results

The inhibition of bacterial growth by HA can be explained by the existence of hydrogen bonds in the hydroxyapatite phase exhibiting hydroxyl groups and the cell wall of bacteria formed by peptidoglycan. When hydrogen bonding occurs, the growth of bacterial cell walls is disrupted, and the bacteria have their development compromised. However, the low amount of hydroxyl groups in the structure of HA does not give the material a 100% antimicrobial property [68]. In the case of cerium containing samples, the mechanisms of metal antibacterial activity are still not completely understood. Díaz-Visurraga et al. (2011) [69] suggest four hypothetical mechanisms that are the most accepted and reported in the literature: (1) the absorption of metallic ions, (2) the generation of reactive oxygen species (ROS) from metal ions with subsequent oxidative damage in their cellular structures, (3) the generation of reactive oxygen species (ROS) from metal ions, and (4) the accumulation of metal ion dissolution in the bacterial membrane causing changes in its permeability (progressive release of lipopolysaccharides, membrane proteins) by the dissipation of the proton motive force.

Ciobanu et al. [39] studied the antimicrobial activity of cerium-containing hydroxyapatite with Ce^{+4} and Ce^{3+} ions and found significant activity against *E. coli* and *S. aureus* by the disc diffusion method. In their work, the hydroxyapatite substituted with 10% cerium has shown a microbial reduction of 31.38% for *E. coli* and 29.01% for *S. aureus*. The results have shown that the activity presented by the material with 5.00% cerium is superior to that in the mentioned article, besides presenting a greater response against *S. aureus*. This confirmed that cerium may improve the antimicrobial activity of HA when substituted in its structure in addition to having osteogenic properties.

The lower inhibition response of cerium to *E. coli* may be related to the fact that the cell wall structure of Gram-negative bacteria is more complex than that of Gram-positive bacteria. This is because there is a layer beyond peptidoglycan named the outer membrane which is composed mainly of phospholipids and lipopolysaccharides. One of the functions of the outer membrane is to protect the bacterial cell [70,71]. Infections in the implants are usually caused by the Gram-positive *S. aureus* bacteria. A survey described by Trampuz and Zimmerli [72] showed that about 30% of cases of implant-related infections were caused by *S. aureus* as it is responsible for soft tissue infections in osteoarticular regions. This is an important result in view of the 42.86% increase in the inhibitory effect against *S. aureus* for Ce-HA.

The calcium dosage revealed that there is a tendency in calcium reduction, after the groups in this study underwent ovariectomy. The CC and Ce-HA-OVX groups present significant differences when compared to the SC (positive control). However, the groups that were submitted to OVX do not present significant differences, which shows that the result is satisfactory. Thus, the calcium dosage allowed one to infer that the induction of OVX osteoporosis occurred in a desirable way, that is, these results indicate that the process of the induction of osteoporosis has proceeded satisfactorily. Raman spectra indicate that the 30 days Ce-HA-OVX group show successful bone mineralization and that the highest peak intensity of 960 cm^{-1} may be associated with increased calcium deposition and significant bone maturation. This allows one to point out that Ce-HA potentiates the process of osteogenesis in defects caused by osteoporosis.

The hydroxyapatite concentration in the BONE group (reference group) was higher (CLOT < SHAM < Ce-HA-OVX < BONE), since there was a growing increase in phosphate in the studied area, in both periods of time, according to Figure 6b,d. The bone peak

intensity neoformed at 960 cm^{-1} (Figure 6), which suggests that the Ce-HA-OVX group shows statistically superior bone formation to the SC group. These results demonstrate that the groups that received the Ce-HA have higher potential for bone regeneration.

In the histological analysis, it was observed that in all the groups and stages of experimentation there was subperiosteal and subendosteal bone neoformation with consequent filling of the defect with slight variations in remodeling and maturation between groups. In the studied groups, no formation of bone tissue with secondary lamellar (mature) organizational pattern was observed and the reabsorption of Ce-Ha did not occur completely, since vestiges of the implanted material were detected. The work of Adrielle et al. [73], which consisted of evaluating bone repair after in vivo studies of a scaffold consisting of norbixin, demonstrated through histology that the neoformed bone cells for the group that had its defect filled with the material, presented more organized tissue formation with lamellar aspect. However, for the group without the material applied to the osseous defect, areas with inflammation and with little bone formation were observed within a period of 15 days.

Similar to that mentioned, the study by Li et al. [74] which aimed to evaluate bone repair in osteoporotic rats induced after the application of calcium phosphate incorporated with lithium, the histology revealed that the animals that received the material presented significant bone neoformation. On the other hand, the rats without the material had less expressive bone formation, presenting fibrous connective tissue after the period of 30 days [74]. According to the work of Wen et al. [75], which observed bone regeneration in rats after the influence of the simvastatin drug incorporated in Ti-HA, in the histological studies it was verified that the groups that received the composite presented expressive bone neoformation. In contrast, the group where the material containing the drug was not applied showed few cells also for the period of 30 days.

Another study that corroborates our findings is that of Zhou et al. [76]. The authors evaluated bone repair after the implantation of Ti-HA material incorporated with Zn, Mg and Sn. Histological results revealed that the group that underwent the application of the materials had more evident bone neoformation when compared to the groups that did not use the materials, in the period of 90 days. This brief survey of studies related to the incorporation of metal ions in hydroxyapatite lattice reveals that doping with Ce enhances the osteogenic effects of this bioceramic. In other words, we believe there is a capability in which incorporated Ce can regulate the reception and detection of Ca, in order to induce osteogenesis by osteoblastic cells [77,78]. In this way, the literature corroborates the results obtained in the present study.

The micro-CT results obtained in this study are in line with the results described by Xian et al. [79]. The aim of this study was to evaluate the effect on the bone repair of defects in rats after the application of modified hydroxyapatite with osteoprotogerin [79] and also according to the results of the work of Zhou-Shan et al. [80] who observed the administration of a parathyroid hormone together with Sn-Ti-HA implants in rat defects with induced osteoporosis [80]. Thus, the micro-CT images (Figure 8) clearly revealed bone tissue differences between the studied animals, showing evident bone neoformation when compared to the animals of the CC group, after the 30-day period of the implants. This, in an excellent way, corroborates the results presented by the studies presented previously.

Hydroxyapatite is widely used in tissue regeneration and biomedical applications in the form of coatings on metal implants, bone and nerve tissue graft production, drug release agents, wound protection, cell culture substrates, enzymatic immobilization, bone prosthesis and graft coatings due to their excellent biocompatibility, osteoconduction property and similarity with the inorganic components of natural bone [81,82]. Similarity in their periodic trends enables cerium to replace calcium in HA.

In this study, it was possible to observe that by means of doping with the cerium ion, antibacterial properties were promoted without compromising the expected nontoxicity. It was observed that the incorporation of the cerium provided an improvement in the physicochemical and the biological performance of the synthesized materials, which

clearly demonstrated a great potential to be used in bone repair and regeneration, while preventing infection.

5. Conclusions

Hydroxyapatite and cerium-containing hydroxyapatite were successfully synthetized by a chemical precipitation method. These cerium-containing formulations presented a clear bacterial inhibition against Gram-negative and Gram-positive bacterial strains. On the other hand, the addition of cerium ions to the hydroxyapatite lattice significantly increased cell viability. The in vivo studies have shown that the presence of this material can accelerate bone regeneration and that cerium incorporated into hydroxyapatite increases bone neoformation, as clearly demonstrated through Raman spectroscopy, histological and micro-CT analyses. Therefore, the material herein synthesized and studied shows promising properties for applications as a filling material in bone-related diseases, where the stimulation of bone regeneration is need, such as osteoporosis.

Author Contributions: Conceptualization, A.L.M.d.O., A.L.-O., M.G.d.F. and E.C.d.S.-F.; Formal analysis, A.M.-F., A.L.M.d.O. and J.A.O.; Funding acquisition, E.C.d.S.-F.; Investigation, E.V., M.S., D.F., K.R., A.L.M.d.O. and A.C.F.; Methodology, E.V., M.S., D.F. and J.F.-S.; Project administration, A.L.-O. and E.C.d.S.-F.; Resources, E.V., M.S., A.M.-F., J.F.-S. and K.R.; Supervision, A.M.-F. and E.C.d.S.-F.; Validation, A.C.F. and A.L.M.d.O.; Writing—original draft, E.V. and E.C.d.S.-F.; Writing—review & editing, A.L.-O., M.G.d.F., A.L.M.d.O., J.A.O. and E.C.d.S.-F. All authors have read and agreed to the published version of the manuscript.

Funding: This research was funded by CNPq-Brazil grants numbers 306176/2019 and 307460/2016-9.

Institutional Review Board Statement: The study was conducted according to the guidelines and approved by Animal Use Ethics Committee of the State University of Piauí (UESPI) (protocol code 0097/2017 and 10 July 2017.

Informed Consent Statement: Not applicable.

Data Availability Statement: Part of the results of this work generated the patent entitled "*Composição da hidroxiapatita dopada com metais com propriedades antimicrobianas para aplicações como materiais de preenchimento ósseo*"—(**Composition of metal-doped hydroxyapatite with antimicrobial properties for applications as bone graft substitute materials**). This patent order deposited with the National Institute of Industrial Property (INPI) under the number BR 10 2018 009777-6.

Acknowledgments: The authors thank CNPq (306176/2019-0; 307460/2016-9), CAPES, FAPEPI, UFPI and UESPI for financial and/or structural support.

Conflicts of Interest: The authors declare no conflict of interest.

References

1. Hestehave Pedersen, R.; Rasmussen, M.; Overgaard, S.; Ding, M. Effects of P-15 Peptide Coated Hydroxyapatite on Tibial Defect Repair In Vivo in Normal and Osteoporotic Rats. *BioMed Res. Int.* **2015**, *2015*, 1–14. [CrossRef]
2. Sozen, T.; Ozisik, L.; Calik Basaran, N. An overview and management of osteoporosis. *Eur. J. Rheumatol.* **2017**, *4*, 46–56. [CrossRef]
3. Calori, G.M.; Mazza, E.; Colombo, M.; Ripamonti, C. The use of bone-graft substitutes in large bone defects: Any specific needs? *Injury* **2011**, *42*, S56–S63. [CrossRef]
4. Sherman, B.P.; Lindley, E.M.; Turner, A.S.; Seim, H.B.; Benedict, J.; Burger, E.L.; Patel, V.V. Evaluation of ABM/P-15 versus autogenous bone in an ovine lumbar interbody fusion model. *Eur. Spine J.* **2010**, *19*, 2156–2163. [CrossRef]
5. Kolk, A.; Handschel, J.; Drescher, W.; Rothamel, D.; Kloss, F.; Blessmann, M.; Heiland, M.; Wolff, K.D.; Smeets, R. Current trends and future perspectives of bone substitute materials—From space holders to innovative biomaterials. *J. Cranio Maxillofac. Surg.* **2012**, *40*, 706–718. [CrossRef]
6. Aktuğ, S.L.; Durdu, S.; Yalçın, E.; Çavuşoğlu, K.; Usta, M. Bioactivity and biocompatibility of hydroxyapatite-based bioceramic coatings on zirconium by plasma electrolytic oxidation. *Mater. Sci. Eng. C* **2017**, *71*, 1020–1027. [CrossRef]
7. Taktak, R.; Elghazel, A.; Bouaziz, J.; Charfi, S.; Keskes, H. Tricalcium phosphate-Fluorapatite as bone tissue engineering: Evaluation of bioactivity and biocompatibility. *Mater. Sci. Eng. C* **2018**, *86*, 121–128. [CrossRef]
8. Li, M.; Xiong, P.; Yan, F.; Li, S.; Ren, C.; Yin, Z.; Li, A.; Li, H.; Ji, X.; Zheng, Y.; et al. An overview of graphene-based hydroxyapatite composites for orthopedic applications. *Bioact. Mater.* **2018**, *3*, 1–18. [CrossRef]

9. Ribeiro, M.; De Moraes, M.A.; Beppu, M.M.; Garcia, M.P.; Fernandes, M.H.; Monteiro, F.J.; Ferraz, M.P. Development of silk fibroin/nanohydroxyapatite composite hydrogels for bone tissue engineering. *Eur. Polym. J.* **2015**, *67*, 66–77. [CrossRef]
10. Dos Santos, M.V.B.; Osajima, J.A.; Da Silva Filho, E.C. Hidroxiapatita: Suporte para liberação de fármacos e propriedades antimicrobianas. *Cerâmica* **2016**, *62*, 256–265. [CrossRef]
11. Ibrahim, M.Z.; Sarhan, A.A.D.; Yusuf, F.; Hamdi, M. Biomedical materials and techniques to improve the tribological, mechanical and biomedical properties of orthopedic implants—A review article. *J. Alloy. Compd.* **2017**, *714*, 636–667. [CrossRef]
12. Yilmaz, B.; Alshemary, A.Z.; Evis, Z. Co-doped hydroxyapatites as potential materials for biomedical applications. *Microchem. J.* **2019**, *144*, 443–453. [CrossRef]
13. Avci, M.; Yilmaz, B.; Tezcaner, A.; Evis, Z. Strontium doped hydroxyapatite biomimetic coatings on Ti6Al4V plates. *Ceram. Int.* **2017**, *43*, 9431–9436. [CrossRef]
14. Reger, N.C.; Kundu, B.; Balla, V.K.; Bhargava, A.K. In vitro cytotoxicity and ion release of multi-ion doped hydroxyapatite. *Int. J. Appl. Ceram. Technol.* **2019**, *16*, 503–516. [CrossRef]
15. Kim, H.; Mondal, S.; Bharathiraja, S.; Manivasagan, P.; Moorthy, M.S.; Oh, J. Optimized Zn-doped hydroxyapatite/doxorubicin bioceramics system for efficient drug delivery and tissue engineering application. *Ceram. Int.* **2018**, *44*, 6062–6071. [CrossRef]
16. Ren, F.; Leng, Y.; Xin, R.; Ge, X. Synthesis, characterization and ab initio simulation of magnesium-substituted hydroxyapatite. *Acta Biomater.* **2010**, *6*, 2787–2796. [CrossRef]
17. Yang, H.W.; Lin, M.H.; Xu, Y.Z.; Shang, G.W.; Wang, R.R.; Chen, K. Osteogenesis of bone marrow mesenchymal stem cells on strontium-substituted nano-hydroxyapatite coated roughened titanium surfaces. *Int. J. Clin. Exp. Med.* **2015**, *8*, 257–264.
18. Kumar, V.B.; Khajuria, D.K.; Karasik, D.; Gedanken, A. Silver and gold doped hydroxyapatite nanocomposites for enhanced bone regeneration. *Biomed. Mater.* **2019**, *14*, 1–22. [CrossRef]
19. Hu, Y.; Du, Y.; Jiang, H.; Jiang, G.S. Cerium promotes bone marrow stromal cells migration and osteogenic differentiation via Smad1/5/8 signaling pathway. *Int. J. Clin. Exp. Pathol.* **2014**, *7*, 5369–5378.
20. Priyadarshini, B.; Anjaneyulu, U.; Vijayalakshmi, U. Preparation and characterization of sol-gel derived Ce^{4+} doped hydroxyapatite and its in vitro biological evaluations for orthopedic applications. *Mater. Des.* **2017**, *119*, 446–455.
21. Zhou, G.; Gu, G.; Li, Y.; Zhang, Q.; Wang, W.; Wang, S.; Zhang, J. Effects of cerium oxide nanoparticles on the proliferation, differentiation, and mineralization function of primary osteoblasts in vitro. *Biol. Trace Elem. Res.* **2013**, *153*, 411–418. [CrossRef]
22. Rajeshkumar, S.; Naik, P. Synthesis and biomedical applications of Cerium oxide nanoparticles—A Review. *Biotechnol. Rep.* **2018**, *17*, 1–5. [CrossRef]
23. Schmidlin, P.R.; Tchouboukov, A.; Wegehaupt, F.J.; Weber, F.E. Effect of cerium chloride application on fibroblast and osteoblast proliferation and differentiation. *Arch. Oral Biol.* **2012**, *57*, 892–897. [CrossRef] [PubMed]
24. Phantai, P.; Futalan, C.M.; Utara, S.; Khemthong, P.; Kamonwannasit, S. Structural characterization of cerium-containing hydroxyapatite nanoparticles synthesized by an ultrasonic-assisted sol-gel technique. *Results Phys.* **2018**, *10*, 956–963. [CrossRef]
25. Pandey, A.; Midha, S.; Sharma, R.K.; Maurya, R.; Nigam, V.K.; Ghosh, S.; Balani, K. Antioxidant and antibacterial hydroxyapatite-based biocomposite for orthopedic applications. *Mater. Sci. Eng. C* **2018**, *88*, 13–24. [CrossRef]
26. Singh, R.P.; Singh, M.; Verma, G.; Shukla, S.; Singh, S.; Singh, S. Structural Analysis of Silver Doped Hydroxyapatite Nanopowders by Rietveld Refinement. *Trans. Indian Inst. Met.* **2017**, *70*, 1973–1980. [CrossRef]
27. Othmani, M.; Bachoua, H.; Ghandour, Y.; Aissa, A.; Debbabi, M. Synthesis, characterization and catalytic properties of copper-substituted hydroxyapatite nanocrystals. *Mater. Res. Bull.* **2018**, *97*, 560–566. [CrossRef]
28. Zheng, L.Y.; Zhu, J.F. Study on antimicrobial activity of chitosan with different molecular weights. *Carbohydr. Polym.* **2003**, *54*, 527–530. [CrossRef]
29. Dos Santos Tavares, D.; Resende, C.X.; Quitan, M.P.; De Oliveira Castro, L.; Granjeiro, J.M.; De Almeida Soares, G. Incorporation of strontium up to 5 mol. (%) to hydroxyapatite did not affect its cytocompatibility. *Mater. Res.* **2011**, *14*, 456–460. [CrossRef]
30. Khajuria, D.K.; Razdan, R.; Mahapatra, D.R. Description of a new method of ovariectomy in female rats. *Rev. Bras. Reum.* **2012**, *52*, 462–470.
31. Maia F, A.L.M.; Da Silva, J.L.; Do Amaral, F.P.M.; Martin, A.A.; Lobo, A.O.; Soares, L.E.S. Morphological and chemical evaluation of bone with apatite-coated Al 2O3 implants as scaffolds for bone repair. *Ceramica* **2013**, *59*, 533–538. [CrossRef]
32. Ding, Q.; Qu, Y.; Shi, K.; He, X.; Chen, Z.; Yang, Y.; Wang, X.; Qian, Z. Preparation of bone marrow mesenchymal stem cells combined with Hydroxyapatite/Poly(D,L-lactide) porous microspheres for bone regeneration in calvarial defects. *ACS Appl. Bio Mater.* **2018**, *1*, 1084–1093. [CrossRef]
33. Kurtjak, M.; Vukomanović, M.; Suvorov, D. Antibacterial nanocomposite of functionalized nanogold and gallium-doped hydroxyapatite. *Mater. Lett.* **2017**, *193*, 126–129. [CrossRef]
34. Momma, K.; Izumi, F. VESTA 3 for three-dimensional visualization of crystal, volumetric and morphology data. *J. Appl. Cryst.* **2011**, *44*, 1272–1276. [CrossRef]
35. Vieira, E.G.; Sousa, P.A.A.; Matos, J.M.E.; Santos, M.R.M.C. Síntese pelo método da coprecipitação e caracterização estrutural do tungstato de cálcio com estrutura tipo scheelita. *Cerâmica* **2013**, *59*, 417–425. [CrossRef]
36. Cavalcante, L.S.; Longo, V.M.; Sczancoski, J.C.; Almeida, M.A.P.; Batista, A.A.; Varela, J.A.; Orlandi, M.O.; Longo, E.; Li, M.S. Electronic structure, growth mechanism and photoluminescence of CaWO 4 crystals. *CrystEngComm* **2012**, *14*, 853–868. [CrossRef]
37. Kebiroglu, M.H.; Orek, C.; Bulut, N.; Kaygili, O.; Keser, S.; Ates, T. Temperature dependent structural and vibrational properties of hydroxyapatite: A theoretical and experimental study. *Ceram. Int.* **2017**, *43*, 15899–15904. [CrossRef]

38. Manoj, M.; Subbiah, R.; Mangalaraj, D.; Ponpandian, N.; Viswanathan, C.; Park, K. Influence of Growth Parameters on the Formation of Hydroxyapatite (HAp) Nanostructures and Their Cell Viability Studies. *Nanobiomedicine* **2015**, *2*, 1–11. [CrossRef]
39. Ciobanu, G.; Maria Bargan, A.; Luca, C. *New Cerium(IV)-Substituted Hydroxyapatite Nanoparticles: Preparation and Characterization*; Elsevier: Amsterdam, The Netherlands, 2015; Volume 41.
40. Lei, Y.; Xu, Z.; Ke, Q.; Yin, W.; Chen, Y.; Zhang, C.; Guo, Y. Strontium hydroxyapatite/chitosan nanohybrid scaffolds with enhanced osteoinductivity for bone tissue engineering. *Mater. Sci. Eng. C* **2017**, *72*, 134–142. [CrossRef]
41. Samani, S.; Shokrgozar, M.A.; Kundu, S.C.; Reis, R.L.; Fatahi, Y.; Kaplan, D.L. Silk fibroin/hydroxyapatite composites for bone tissue engineering. *Biotechnol. Adv.* **2018**, *36*, 68–91.
42. Kaygili, O.; Dorozhkin, S.V.; Keser, S. Synthesis and characterization of Ce-substituted hydroxyapatite by sol-gel method. *Mater. Sci. Eng. C* **2014**, *42*, 78–82. [CrossRef]
43. Ren, Y.; Zhou, H.; Nabiyouni, M.; Bhaduri, S.B. Rapid coating of AZ31 magnesium alloy with calcium deficient hydroxyapatite using microwave energy. *Mater. Sci. Eng. C* **2015**, *49*, 364–372. [CrossRef]
44. Kanchana, P.; Navaneethan, M.; Sekar, C. Fabrication of Ce doped hydroxyapatite nanoparticles based non-enzymatic electrochemical sensor for the simultaneous determination of norepinephrine, uric acid and tyrosine. *Mater. Sci. Eng. B Solid-State Mater. Adv. Technol.* **2017**, *226*, 132–140. [CrossRef]
45. Yang, Y.C.; Chen, C.C.; Wang, J.B.; Wang, Y.C.; Lin, F.H. *Flame Sprayed Zinc Doped Hydroxyapatite Coating with Antibacterial and Biocompatible Properties*; Elsevier: Amsterdam, The Netherlands, 2017; Volume 43, ISBN 8862277121.
46. Al-Hazmi, F.E. Synthesis and electrical properties of Bi doped hydroxyapatite ceramics. *J. Alloy. Compd.* **2016**, *665*, 119–123. [CrossRef]
47. Malakauskaite-Petruleviciene, M.; Stankeviciute, Z.; Niaura, G.; Garskaite, E.; Beganskiene, A.; Kareiva, A. Characterization of sol-gel processing of calcium phosphate thin films on silicon substrate by FTIR spectroscopy. *Vib. Spectrosc.* **2016**, *85*, 16–21. [CrossRef]
48. Anwar, A.; Akbar, S. Continuous microwave assisted flow synthesis and characterization of calcium deficient hydroxyapatite nanorods. *Adv. Powder Technol.* **2018**, *29*, 1493–1498. [CrossRef]
49. Hassannejad, H.; Moghaddasi, M.; Saebnoori, E.; Baboukani, A.R. Microstructure, deposition mechanism and corrosion behavior of nanostructured cerium oxide conversion coating modified with chitosan on AA2024 aluminum alloy. *J. Alloys Compd.* **2017**, *725*, 968–975. [CrossRef]
50. Harish, B.M.; Rajeeva, M.P.; Chaturmukha, V.S.; Suresha, S.; Jayanna, H.S.; Yallappa, S.; Lamani, A.R. Influence of zinc on the structural and electrical properties of cerium oxide nanoparticles. *Mater. Today Proc.* **2018**, *5*, 3070–3077. [CrossRef]
51. Zhang, j.; Wong, H.; Yu, D.; Kakushima, K.; Iwai, H. X-ray photoelectron spectroscopy study of high-k CeO_2/La_2O_3 stacked dielectrics. *API Adv.* **2014**, *4*, 1–9. [CrossRef]
52. Murugan, R.; Vijayaprasath, G.; Ravi, G. The influence of substrate temperature on the optical and micro structural properties of cerium oxide thin films deposited by RF sputtering. *Superlattice Microst.* **2015**, *85*, 321–330. [CrossRef]
53. Bêche, E.; Charvin, P.; Perarnau, D.; Abanades, S.; Flamant, G. Ce 3d XPS investigation of cerium oxides and mixed cerium oxide ($Ce_xTi_yO_z$). *Surf Interface Anal.* **2008**, *40*, 264–267. [CrossRef]
54. Guo, B.; Sun, Y.; Finne-Wistrand, A.; Mustafa, K.; Albertsson, A.C. Electroactive porous tubular scaffolds with degradability and non-cytotoxicity for neural tissue regeneration. *Acta Biomater.* **2012**, *8*, 144–153. [CrossRef]
55. Branco, A.C.S.C.; Diniz, M.F.F.M.; Almeida, R.N.; Santos, H.B.; Oliveira, K.M. Parâmetros Bioquímicos e Hematológicos de Ratos Wistar e Camundongos Swiss do Biotério Professor Thomas George Biochemical and Hematological Parameters of Wistar Rats and Swiss Mice in the Professor Thomas George Animal Laboratory. *Pesqui. Res.* **2011**, *15*, 209–214.
56. Suenaga, H.; Furukawa, K.S.; Suzuki, Y.; Takato, T.; Ushida, T. Bone regeneration in calvarial defects in a rat model by implantation of human bone marrow-derived mesenchymal stromal cell spheroids. *J. Mater. Sci. Mater. Med.* **2015**, *26*, 1–9. [CrossRef]
57. Lopes, C.B.; Pacheco, M.T.T.; Silveira, L.; Cangussú, M.C.T.; Pinheiro, A.L.B. The effect of the association of near infrared laser therapy, bone morphogenetic proteins, and guided bone regeneration on tibial fractures treated with internal rigid fixation: A Raman spectroscopic study. *J. Biomed. Mater. Res. Part A* **2010**, *94*, 1257–1263. [CrossRef]
58. Sang Cho, J.; Um, S.H.; Su Yoo, D.; Chung, Y.C.; Hye Chung, S.; Lee, J.C.; Rhee, S.H. Enhanced osteoconductivity of sodium-substituted hydroxyapatite by system instability. *J. Biomed. Mater. Res. Part B Appl. Biomater.* **2014**, *102*, 1046–1062. [CrossRef]
59. Lin, Y.; Yang, Z.; Cheng, J. Preparation, Characterization and Antibacterial Property of Cerium Substituted Hydroxyapatite Nanoparticles. *J. Rare Earths* **2007**, *25*, 452–456. [CrossRef]
60. Sobczak-Kupiec, A.; Olender, E.; Malina, D.; Tyliszczak, B. Effect of calcination parameters on behavior of bone hydroxyapatite in artificial saliva and its biosafety. *Mater. Chem. Phys.* **2018**, *206*, 158–165. [CrossRef]
61. Jazayeri, H.E.; Tahriri, M.; Razavi, M.; Khoshroo, K.; Fahimipour, F.; Dashtimoghadam, E.; Almeida, L.; Tayebi, L. A current overview of materials and strategies for potential use in maxillofacial tissue regeneration. *Mater. Sci. Eng. C* **2017**, *70*, 913–929. [CrossRef]
62. Bohner, M.; Galea, L.; Doebelin, N. Calcium phosphate bone graft substitutes: Failures and hopes. *J. Eur. Ceram. Soc.* **2012**, *32*, 2663–2671. [CrossRef]
63. Arifta, T.I.; Munar, M.L.; Tsuru, K.; Ishikawa, K. Fabrication of interconnected porous calcium-deficient hydroxyapatite using the setting reaction of α tricalcium phosphate spherical granules. *Ceram. Int.* **2017**, *43*, 11149–11155. [CrossRef]

64. Okada, M.; Matsumoto, T. Synthesis and modification of apatite nanoparticles for use in dental and medical applications. *Jpn. Dent. Sci. Rev.* **2015**, *51*, 85–95. [CrossRef]
65. Pourbaix, M. *Atlas of Electrochemical Equilibria in Aqueous Solutions*, 1st ed.; Pergamon Press: Oxford, UK, 1966.
66. Arenas, L.F.; Ponce De León, C.; Walsh, F.C. Electrochemical redox processes involving soluble cerium species. *Electrochim. Acta* **2016**, *205*, 226–247. [CrossRef]
67. Chen, Y.; Qiu, C.; Chen, C.; Fan, X.; Xu, S.; Guo, W.; Wang, Z. Facile synthesis of ceria nanospheres by $Ce(OH)CO_3$ precursors. *Mater. Lett.* **2014**, *122*, 90–93. [CrossRef]
68. Katsikogianni, M.; Missirlis, Y.F.; Harris, L.; Douglas, J. Concise review of mechanisms of bacterial adhesion to biomaterials and of techniques used in estimating bacteria-material interactions. *Eur. Cells Mater.* **2004**, *8*, 37–57. [CrossRef]
69. Gutiérrez, C.; Von Plessing, C.; García, A. Metal nanostructures as antibacterial agents. *Sci. Against Microb. Pathog. Commun. Curr. Res. Technol. Adv.* **2011**, *3*, 210–218.
70. Babenko, L.P.; Zholobak, N.M.; Shcherbakov, A.B.; Voychuk, S.I.; Lazarenko, L.M.; Spivak, M.Y. Antibacterial activity of cerium colloids against opportunistic microorganisms in vitro. *Mikrobiol. Z.* **2012**, *74*, 54–62. [PubMed]
71. Ouyang, Y.; Xie, Y.; Tan, S.; SHI, Q.; Chen, Y. Structure and antibacterial activity of Ce^{3+} exchanged montmorillonites. *J. Rare Earths* **2009**, *27*, 858–863. [CrossRef]
72. Trampuz, A.; Zimmerli, W. Diagnosis and treatment of infections associated with fracture-fixation devices. *Injury* **2006**, *37*, 59–66. [CrossRef]
73. Alves, A.M.M.; de Miranda Fortaleza, L.M.; Filho, A.L.M.M.; Ferreira, D.C.L.; da Costa, C.L.S.; Viana, V.G.F.; Santos, J.Z.L.V.; de Oliveira, R.A.; de Meira Gusmão, G.O.; Soares, L.E.S. Evaluation of bone repair after application of a norbixin membrane scaffold with and without laser photobiomodulation (λ 780 nm). *Lasers Med. Sci.* **2018**, *33*, 1493–1504. [CrossRef]
74. Li, L.; Peng, X.; Qin, Y.; Wang, R.; Tang, J.; Cui, X.; Wang, T.; Liu, W.; Pan, H.; Li, B. Acceleration of bone regeneration by activating Wnt/β-catenin signalling pathway via lithium released from lithium chloride/calcium phosphate cement in osteoporosis. *Sci. Rep.* **2017**, *7*, 1–12. [CrossRef] [PubMed]
75. Fang, W.; Zhao, S.; He, F.; Liu, L.; Yang, G. Influence of simvastatin-loaded implants on osseointegration in an ovariectomized animal model. *Biomed. Res. Int.* **2015**, *2015*, 1–8. [CrossRef] [PubMed]
76. Tao, Z.S.; Zhou, W.S.; He, X.W.; Liu, W.; Bai, B.L.; Zhou, Q.; Huang, Z.L.; Tu, K.K.; Li, H.; Sun, T.; et al. A comparative study of zinc, magnesium, strontium-incorporated hydroxyapatite-coated titanium implants for osseointegration of osteopenic rats. *Mater. Sci. Eng. C* **2016**, *62*, 226–232. [CrossRef] [PubMed]
77. Canalis, E.; Hott, M.; Deloffre, P.; Tsouderos, Y.; Marie, P.J. The divalent strontium salt S12911 enhances bone cell replication and bone formation in vitro. *Bone* **1996**, *18*, 517–523. [CrossRef]
78. Chandran, S.; Suresh Babu, S.; Hari Krishnan, V.S.; Varma, H.K.; John, A. Osteogenic efficacy of strontium hydroxyapatite micro-granules in osteoporotic rat model. *J. Biomater. Appl.* **2016**, *31*, 499–509. [CrossRef]
79. Liu, X.; Bao, C.; Xu, H.H.K.; Pan, J.; Hu, J.; Wang, P.; Luo, E. Osteoprotegerin Gene-Modified BMSCs with Hydroxyapatite Scaffold for Treating Critical-Sized Mandibular Defects in Ovariectomized Osteoporotic Rats. *Acta Biomater.* **2016**, *42*, 378–388. [CrossRef]
80. Tao, Z.S.; Zhou, W.S.; Qiang, Z.; Tu, K.K.; Huang, Z.L.; Xu, H.M.; Sun, T.; Lv, Y.X.; Cui, W.; Yang, L. Intermittent administration of human parathyroid hormone (1–34) increases fixation of strontium-doped hydroxyapatite coating titanium implants via electrochemical deposition in ovariectomized rat femur. *J. Biomater. Appl.* **2016**, *30*, 952–960. [CrossRef]
81. Sadat-Shojai, M.; Khorasani, M.T.; Dinpanah-Khoshdargi, E.; Jamshidi, A. Synthesis methods for nanosized hydroxyapatite with diverse structures. *Acta Biomater.* **2013**, *9*, 7591–7621. [CrossRef]
82. Lin, K.; Wu, C.; Chang, J. Advances in synthesis of calcium phosphate crystals with controlled size and shape. *Acta Biomater.* **2014**, *10*, 4071–4102. [CrossRef] [PubMed]